catalysts

MDPI

Article

A Novel Metal–Organic Framework Route to Embed Co Nanoparticles into Multi-Walled Carbon Nanotubes for Effective Oxygen Reduction in Alkaline Media

Hong Zhu *, Ke Li, Minglin Chen, Hehuan Cao and Fanghui Wang

State Key Laboratory of Chemical Resource Engineering, Institute of Modern Catalysis, Department of Organic Chemistry, School of Science, Beijing University of Chemical Technology, Beijing 100029, China; like200933@163.com (K.L.); chml24@163.com (M.C.); 2016410013@mail.buct.edu.cn (H.C.); fhwang@mail.buct.edu.cn (F.W.)

* Correspondence: zhuho128@126.com; Tel.: +86-10-6444-4919

Received: 1 November 2017; Accepted: 23 November 2017; Published: 27 November 2017

Abstract: Metal–organic framework (MOF) materials can be used as precursors to prepare non-precious metal catalysts (NPMCs) for oxygen reduction reaction (ORR). Herein, we prepared a novel MOF material (denoted as Co-bpdc) and then combined it with multi-walled carbon nanotubes (MWCNTs) to form Co-bpdc/MWCNTs composites. After calcination, the cobalt ions from Co-bpdc were converted into Co nanoparticles, which were distributed in the graphite carbon layers and MWCNTs to form Co-bpdc/MWCNTs. The prepared catalysts were characterized by TEM (Transmission electron microscopy), XRD (X-ray diffraction), XPS (X-ray photoelectron spectroscopy), BET (Brunauer–Emmett–Teller), and Raman spectroscopy. The electrocatalytic activity was measured by using rotating disk electrode (RDE) voltammetry. The catalysts showed higher ORR catalytic activity than the commercial Pt/C catalyst in alkaline solution. Co-bpdc/MWCNTs-100 showed the highest ORR catalytic activity, with an initial reduction potential and half-wave potential reaching 0.99 V and 0.92 V, respectively. The prepared catalysts also showed superior stability and followed the 4-electron pathway ORR process in alkaline solution.

Keywords: metal–organic framework; non-precious metal catalyst; oxygen reduction reaction; Co-bpdc; Co-bpdc/MWCNTs composites

1. Introduction

In recent years, as a result of the global energy crisis and environmental pollution, the search for cheap, efficient, and environmentally friendly alternative energy conversion and storage systems has aroused huge and sustained interest [1,2]. Hydrogen is a clean energy source, and fuel cells are the best way to utilize it. Fuel cells are considered one of the most efficient clean power-generating technologies of the 21st century. However, the high cost of fuel cells limits their commercialization; the precious metal catalysts make up a large part of the cost. To realize commercialization of the fuel cells as soon as possible, we urgently need to develop high-efficiency and low-cost non-precious metal catalysts to replace the high-cost, platinum-based noble metal catalysts [3–7].

Oxygen reduction reaction (ORR) plays a pivotal role in fuel cells and metal–air batteries [8–10]. Among the various non-noble metal ORR catalysts, transition metal–nitrogen–carbon (M/N/C) complexes or composites have attracted much attention due to their low price, high activity, long durability, and high resistance to methanol exchange [11,12]. Over the past several decades, non-noble metal catalysts (mainly Fe or Co) have been the most studied and have made great progress [13–17]. Jasinski first reported that nitrogen-containing metal macrocyclic compounds were able to catalyze oxygen reduction reaction, and thus created a new era of non-precious metals and

non-metallic catalysts [10]. Subsequent studies have found that the activity and stability of the catalyst can be improved by pyrolyzing the metal salt compound and the nitrogen macrocyclic compound, which contain transition metal, nitrogen source, and carbon source [17–19]. Furthermore, the heteroatom-doped carbon material is a kind of promising material that can be used to replace the noble metal catalyst, and the doping of the carbon material with heteroatoms can effectively improve electrocatalytic activity and stability [20–22]. Among the heteroatom-doped carbon materials, nitrogen-doped carbon nanomaterials have been extensively studied because of their low cost, high electrocatalytic activity, high durability, and good environmental protection [23–25]. Many results have shown that the introduction of nitrogen atoms can induce the ionization of adjacent carbon atoms, promote the adsorption of oxygen, and lead to the improvement of catalytic activity. Nitrogen-doped carbon materials can also work with metal compounds to significantly improve catalytic efficiency [21,26].

Metal–organic framework (MOF) materials are composed of inorganic metal centers (metal ions or metal clusters) and bridged organic ligands through self-assembly interconnection, forming a porous crystalline material with a cyclical network structure [27–30]. MOF materials have a great prospect in non-precious metal catalysts because MOF materials have many advantages, such as structural diversity, adjustable aperture, and large specific surface area. These advantages have attracted the attention of researchers, and make MOF materials widely used in the catalytic field [29,31–33]. Since MOF-derived catalysts have many fully exposed nanostructures, resulting in their excellent electron transport properties, these catalysts have high electrocatalytic activity in fuel cells, in both acidic and alkaline electrolytes [29,34]. We can modify a MOF material to make it rich in Fe–N_4 or Co–N_4 coordination structure, so that the MOF material contains transition metal, nitrogen source, and carbon source. Specifically, we can introduce nitrogen atoms to form nitrogen-containing organic ligands, and then coordinate the modified ligands with the transition metal ions, to form a new kind of MOF material that contains nitrogen [30,33,34].

2. Results

Herein, we reported a novel MOF material (denoted as Co-bpdc) and the preparation of Co-bpdc/MWCNTs composites. The Co-bpdc and Co-bpdc/MWCNTs composites were heated at a high temperature in a N_2 atmosphere to form the catalysts. After calcination, the structure of the Co-bpdc/MWCNTs composites was destroyed, and the organic ligands from the Co-bpdc were carbonized to the graphite carbon layer. The central cobalt ions from the Co-bpdc were converted into Co nanoparticles, which were then distributed in the graphite carbon layers and MWCNTs. The MWCNTs worked as carriers and helped to disperse the cobalt atoms, and the addition of MWCNTs also improved the conductivity and electrocatalytic activity of the catalysts. For all the above reasons, the prepared catalysts have a higher ORR catalytic activity than the commercial Pt/C catalyst in alkaline media.

Formatting of Mathematical Components. The electron transfer number (n) during the oxygen reduction reaction was calculated from the Koutecky–Levich equation:

$$\frac{1}{J} = \frac{1}{J_L} + \frac{1}{J_K} = \frac{1}{B\omega^{1/2}} + \frac{1}{J_K} \quad (1)$$

$$B = 0.62nFC_0(D_0)^{2/3}v^{-1/6} \quad (2)$$

$$J_K = nFkC_0 \quad (3)$$

Here, J is the current density, J_L and J_K are the diffusion- and kinetic-limiting current densities, respectively, ω is the angular velocity, F is the Faraday constant (96,485 C mol^{-1}), C_0 is the O_2 bulk concentration ($C_0 = 1.26 \times 10^{-6}$ mol cm^{-3}), D_0 is the diffusion coefficient of the O_2 in 0.1 M KOH or $HClO_4$ ($D_0 = 1.9 \times 10^{-5}$ cm s^{-1}), v is the kinematic viscosity of the electrolyte ($v = 0.1$ m^2 s^{-1} in 0.1 M KOH or $HClO_4$) [35].

Rotating ring-disk electron (RRDE) measurement can verify the ORR catalytic pathways of catalysts. We performed the measurement using a glassy carbon disk with a Pt ring at 0.73 V at a rotating speed of 1600 rpm. The electron transfer number (n) and the peroxide yield (HO^{2-}) during the ORR process can be calculated according the following equation:

$$n = \frac{4I_d}{I_d + \frac{I_r}{N}} \tag{4}$$

$$\%(H_2O_2) = \frac{\frac{200I_r}{N}}{I_d + \frac{I_r}{N}} \tag{5}$$

Here, I_d and I_r are the disk current and ring current, respectively, and N is the current collection efficiency of the Pt ring (0.37) [35].

3. Discussion

Our preparation process of the Co-bpdc/MWCNTs composites is based on the Co-bpdc and MWCNTs. Firstly, phenanthroline was oxidized to 2,2′-bipyridine-3,3′-dicarboxylic acid (H_2bpdc) by potassium permanganate under alkaline conditions. Secondly, the Co-bpdc was synthesized with the cobalt center and 2,2′-bipyridine-3,3′-dicarboxylic acid under acidic conditions with the hydrothermal synthesis. Co-bpdc works as MOF precursors, which provided the transition metal and nitrogen sources. The coordination between cobalt ions and H_2bpdc is shown in Figure 1, and Co-bpdc can also be expressed as $[Co(bpdc)(H_2O)_2]_n$. Secondly, the MWCNTs were introduced during the coordination reaction to obtain Co-bpdc/MWCNTs composites. Finally, the Co-bpdc and Co-bpdc/MWCNTs composites were pyrolyzed by heating at a high temperature in N_2 atmosphere, and then the catalysts were prepared.

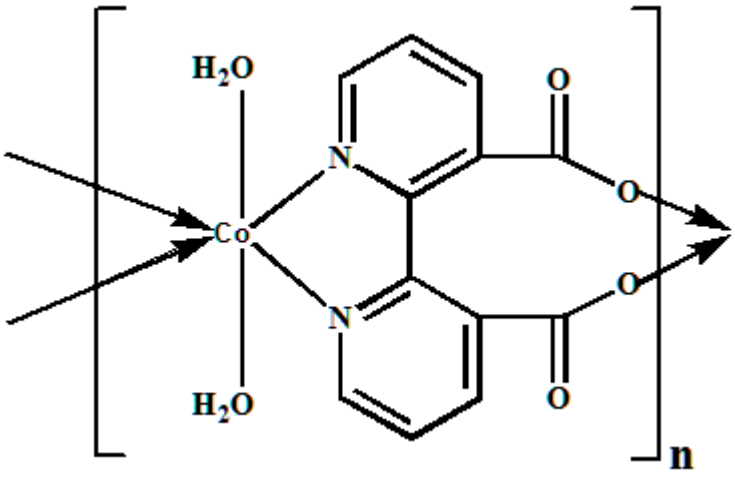

Figure 1. The coordination diagram between cobalt ions and H_2bpdc.

The formation of Co-bpdc and Co-bpdc/MWCNTs composites after calcination was confirmed by X-ray diffraction (XRD), as shown in Figure 2. The characteristic diffraction peak at 26°/2θ belongs to the (002) plane of the graphitic carbon in the MWCNTs, consistent with the results in the literature [35]. The (100) plane of the graphitic carbon in the prepared catalysts disappeared, and the (002) plane of graphitic carbon intensity in all the prepared catalysts was lower than that of graphitic carbon intensity in MWCNTs, indicating that the introduction of Co-bpdc decreased the graphitization of MWCNTs. In addition, the characteristic diffraction peaks at 44°, 51°, and 75°/2θ belong to the (111), (200), and (220) planes of Co nanoparticles (JCPDS no. 15-0806), indicating that the central cobalt ions from the Co-bpdc and Co-bpdc/MWCNTs have been converted into Co nanoparticles after

calcination. This result proves that the prepared catalysts contain the single crystal face-centered cubic structure [36]. The diffraction peak for Co (220) is used to evaluate the particle size of Co by Scherrer's equation:

$$D = \frac{0.9\lambda}{Bcos\theta} \quad (6)$$

Here, D is average particle size, the wavelength λ is close to 0.154056 nm, θ is the angle of Co (220) peak and B is the full width at half-maximum in radians (FWHM) [37]. The calculated average particle size of Co nanoparticles is 16.54 nm.

To some extent, with the increase of MWCNTs content, more dispersed cobalt particles result in more active sites being exposed, because of the greater dispersion of cobalt particles. When the content of MWCNTs is excessive, the excessive MWCNTs will cover part of active sites, resulting in the reduction of active sites in catalysts.

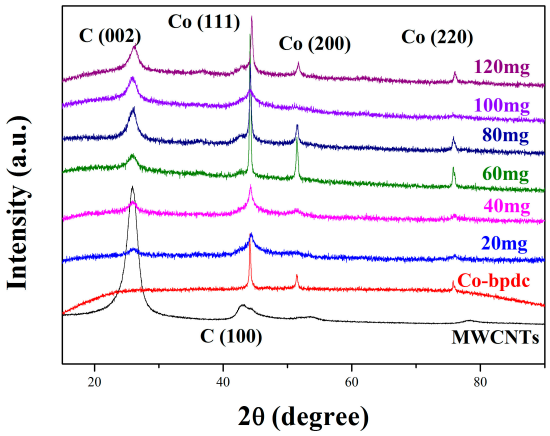

Figure 2. XRD patterns of Co-bpdc/MWCNTs compositions with different contents of MWCNTs.

Figure 3 shows the Raman spectra of MWCNTs and Co-bpdc/MWCNTs composites after calcination. The Raman spectra display the characteristic D band (at about 1345 cm^{-1}) and G band (at about 1590 cm^{-1}) of the carbon in the catalysts [38]. Because the incorporation of heteroatoms (mainly nitrogen) leads to a certain degree of defects in the carbon material, the ratio of the intensity of the D band to that of the G band (I_D/I_G) is used to characterize the defects of the carbon material. Here, the ratio for MWCNTs, reaching 1.09, is the lowest and the ratio for Co-bpdc/MWCNTs-100, reaching 1.64, is the highest among the prepared catalysts. These results indicate that the introduction of Co-bpdc increases the defects of MWCNTs.

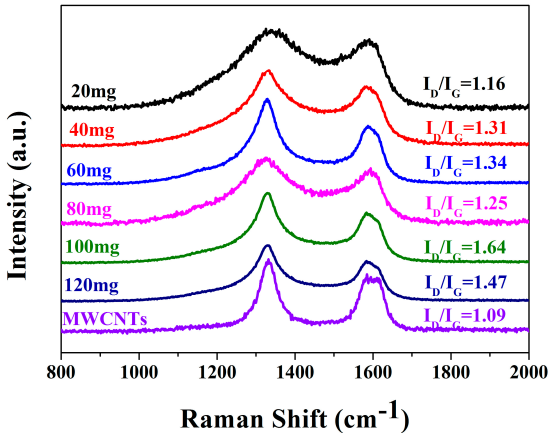

Figure 3. Ramanspectra of Co-bpdc/MWCNTs compositions with different contents of MWCNTs.

Figure 4 exhibits the typical morphology of Co-bpdc and Co-bpdc/MWCNTs composites. The Co-bpdc crystal has a rectangular structure in Figure 4a. The MWCNTs were successfully combined with the Co-bpdc as observed in Figure 4b. After the calcination, Figure 4c,d demonstrates the microstructure of Co-bpdc and Co-bpdc/MWCNT composites. From Figure 4c,d, we found that the structure of Co-bpdc was destroyed and a degree of agglomeration took place. The structure of Co-bpdc/MWCNTs composites was destroyed, and the organic ligands from the Co-bpdc carbonized to the graphite carbon layer. The central cobalt ions from the Co-bpdc were converted into Co nanoparticles, and then the Co nanoparticles were distributed in the graphite carbon layers and MWCNTs. The average particle size of the Co nanoparticles was calculated to be 16.93 nm (Figure 4e), which is close to the XRD result. This result indicates that the addition of MWCNTs can make the cobalt nanoparticles distribute more uniformly, and this structure can contribute to the transmission of oxygen and electrolytes to the catalyst surface. A HRTEM (High-resolution transmission electron microscopy) image of the Co-bpdc/MWCNTs-100 is shown in Figure 4f. As shown in Figure 4f, the metal particle is coated by carbon layers, and the lattice distance of 0.244 nm corresponds to the lattice fringe (111) of Co and is consistent with the XRD results [39].

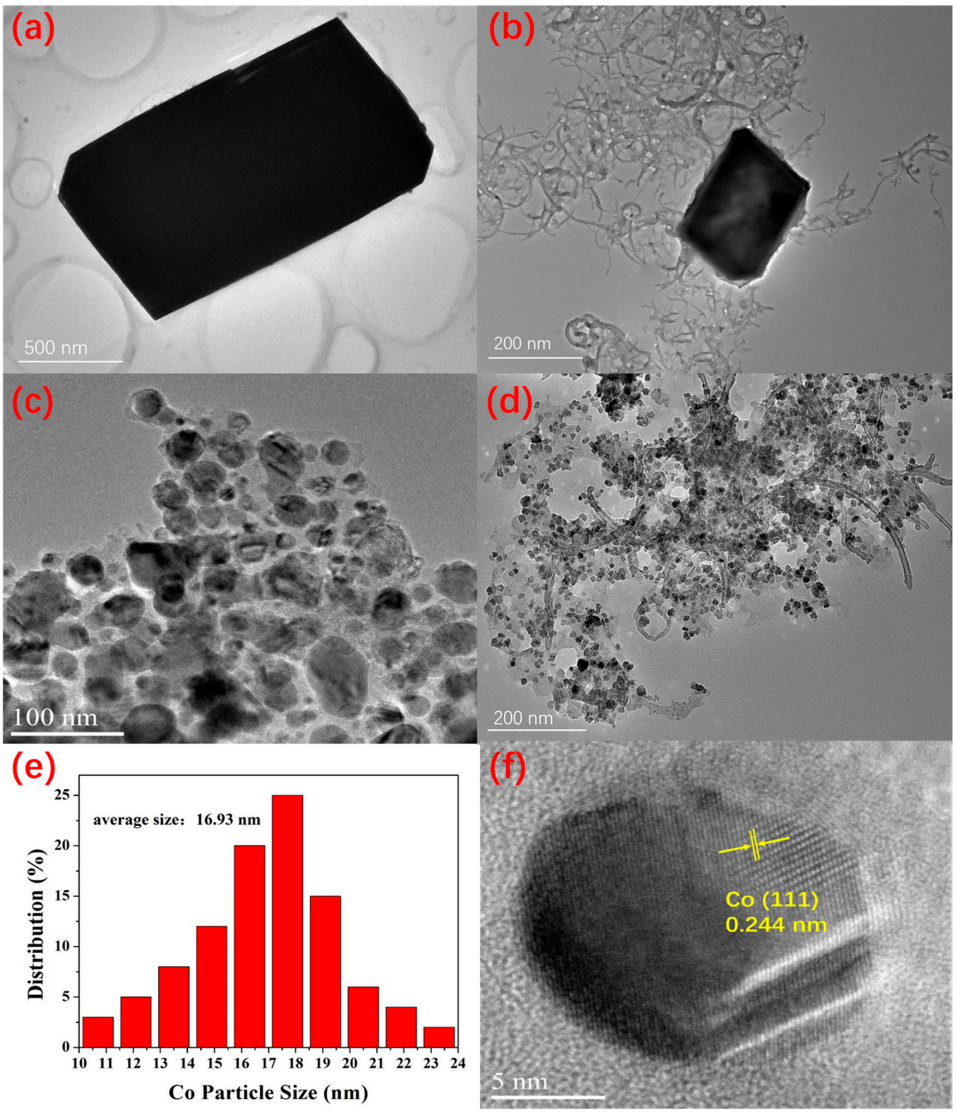

Figure 4. (**a**) TEM image of Co-bpdc; (**b**) TEM image of Co-bpdc/MWCNTs-100; (**c**) TEM image of Co-bpdc after calcination; (**d**) TEM image of Co-bpdc/MWCNTs-100 after calcination; (**e**) particle size distribution of Co-bpdc/MWCNTs-100; and (**f**) HRTEM image of Co-bpdc/MWCNTs-100.

The elemental compositions and valence states of these catalysts were studied by X-ray photoelectron spectroscopy (XPS). Figure 5a reveals the presence of C, N, O, and Co in Co-bpdc/MWCNTs-100. For example, the high-resolution C 1s spectrum is deconvoluted in Figure 5b. The peaks at 284.6 and 285.6 eV are attributed to sp^2-hybridized graphite-like carbon (C–C sp^2) and sp^3-hybridized diamond-like carbon (C–C sp^3), respectively. The peaks at 286.5 and 287.7 eV correspond to C–O/C–N and C=O/C=N, respectively, on the surface of the catalyst, indicating successful N-doping [35,40]. The peak at 290.4 eV belongs to the p-p* shake up satellites of sp^2 graphite-like carbon, indicating the occurrence of aromatization during the carbonization of the catalyst. The N element in the catalysts comes from the organic ligands in the Co-bpdc. The N element in Co-bpdc/MWCNTs-0 is the highest among the prepared catalysts, reaching 3.54 wt %, followed by that in Co-bpdc/MWCNTs-100 (Table 1). The fitted N 1s spectrum of Co-bpdc/MWCNTs-100 in Figure 5c can be deconvoluted to four N species: pyridinic N at 398.2 eV, pyrrolic N at 399.8 eV, graphitic N at 401.2 eV, and oxidized N at 402.5 eV [35]. Figure 5d shows the deconvoluted Co 2p spectrum. The two peaks at 780.5 eV and 795.6 eV correspond to Co $2p_{3/2}$ and Co $2p_{1/2}$, in accordance with the report on Co_3O_4 [35,39]. These results indicate that the element of cobalt appears in the catalysts mainly as cobalt metal and in a small amount as cobalt oxide.

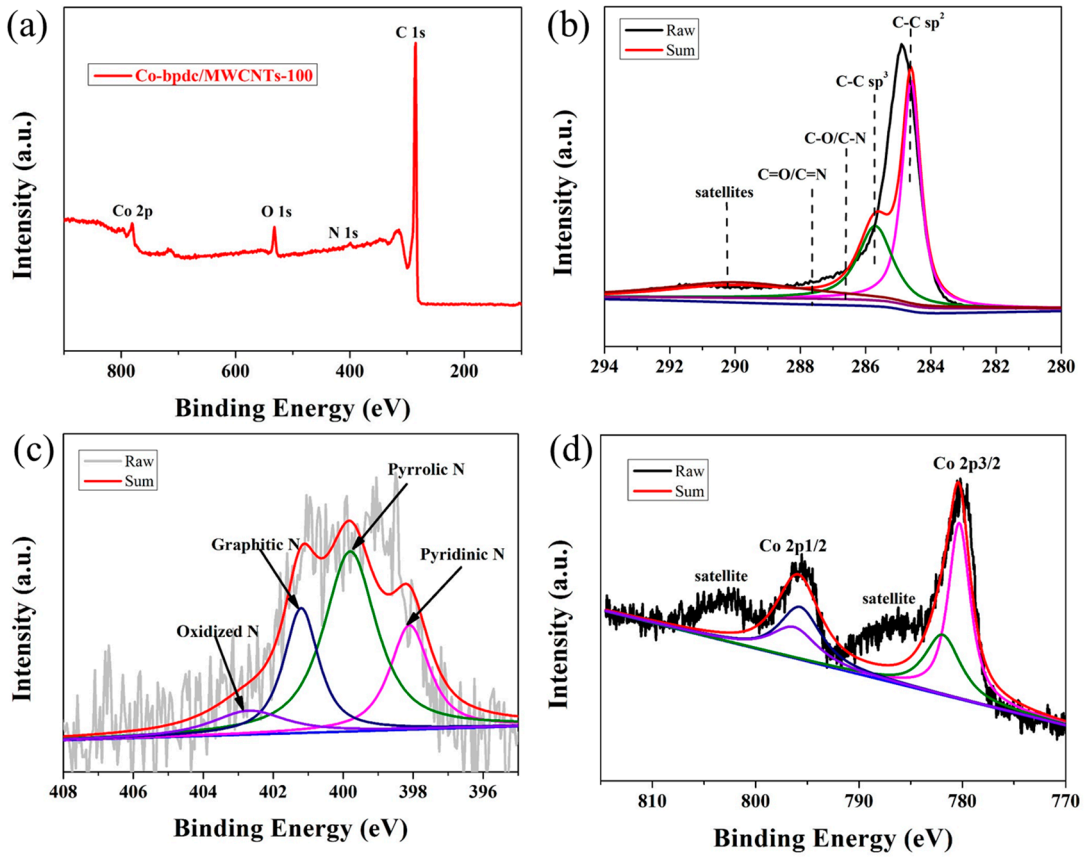

Figure 5. XPS spectra of Co-bpdc/MWCNTs-100: (**a**) Survey scan spectrum; (**b**) deconvoluted C 1s spectrum; (**c**) deconvoluted N 1s spectrum; and (**d**) deconvoluted Co 2p.

Table 1. The proportion of different atoms in Co-bpdc/MWCNTs composites with different contents of MWCNTs.

Elements	0	20	40	60	80	100	120
C	66.65	88.01	89.75	91.05	92.51	91.94	92.67
O	23.79	7.24	6.06	5.65	4.39	4.9	4.79
Co	6.01	3.12	2.35	1.44	1.24	1.14	1.3
N	3.54	1.63	1.84	1.86	1.87	2.02	1.24

From Table 1, we found that the relative content of O, Co and N in the catalysts containing MWCNTs decreases, compared with Co-bpdc. The main reasons are as follows. During the formation of Co-bpdc/MWCNTs composites, MWCNTs are incorporated into Co-bpdc, resulting in Co-bpdc/MWCNTs composites becoming a porous material. After calcination, Co-bpdc/MWCNTs composites were carbonized and the structure of Co-bpdc/MWCNTs composites was destroyed, resulting in a substantial loss of elements in the catalysts. The relative contents of O, Co and N in Co-bpdc were higher than the other catalysts, due to the large amount of agglomeration occurring during calcination. The presence of MWCNTs make Co particles distribute on the MWCNTs more uniformly. Excluding Co-bpdc, with increasing content of MWCNTs, the content of nitrogen in the catalysts first increases, reaching a maximum of 2.02% at 100 mg of MWCNTs, and then drops. However, the trend of Co elements is opposite to the trend of nitrogen elements.

Figure 6 depicts the nitrogen adsorption–desorption isotherm and the corresponding pore-size distribution curve of Co-bpdc/MWCNTs-100. The Brunauer–Emmett–Teller (BET) surface area and the cumulative pore volume of Co-bpdc/MWCNTs-100 are 221.02 m^2 $g^{-1}$and 0.47 cm^3 g^{-1}, respectively. The isotherm is a type IV BET isotherm with a H_3-type hysteresis loop ($P/P_0 > 0.4$), and the pore-size distribution curve shows a wide pore size distribution, ranging from micropores to mesopores, indicating the mesoporous characteristic of the Co-bpdc/MWCNTs-100. This characteristic contributes to the diffusion of oxygen onto the catalyst surface [35]. As a comparison, the BET surface area of Co-bpdc is 92.92 m^2 g^{-1}, which is lower than Co-bpdc/MWCNTs-100. The higher specific surface area means that the catalysts contain more active sites in unit volume, leading to the higher catalytic activity of the corresponding catalyst.

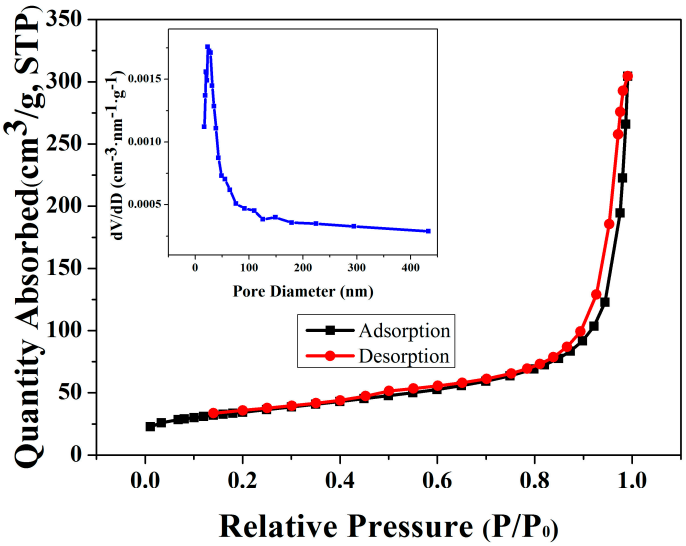

Figure 6. Nitrogen adsorption–desorption isotherm of Co-bpdc/MWCNTs-100.

The electrocatalytic activities of the as-prepared catalysts toward oxygen reduction reaction (ORR) were measured by cyclic voltammetry (CV) and linear sweep voltammetry (LSV) with a

rotating disk electrode (RDE) in 0.1 M KOH solution. In Figure 7a, between 0.1 V and 1.6 V, all the prepared catalysts show a featureless voltammogram current curve in N_2-saturated solution, but a voltammogram with well-defined cathodic peaks in an O_2-saturated solution indicates that the catalysts have good oxygen reduction electrocatalytic activity [19]. The polarization curves of the prepared catalysts and the commercial Pt/C catalyst are shown in Figure 7b. Of all the prepared catalysts, Co-bpdc/MWCNTs-100 exhibits the best electrocatalytic activity toward ORR, and its initial reduction potential and half-wave potential reach 0.99 V and 0.92 V, respectively. The electrocatalytic activity of Co-bpdc/MWCNTs-100 toward ORR is much higher than that of the commercial Pt/C catalyst. Moreover, Co-bpdc/MWCNTs-100 also shows a larger current density than the other catalysts. On the other hand, Co-bpdc/MWCNTs-0 exhibits the worst electrocatalytic activity, and its initial reduction potential and half-wave potential reaches 0.90 V and 0.87 V, respectively, indicating that the introduction of MWCNTs can enhance the electrocatalytic activity. This result confirms that the higher specific areas of catalysts mean higher catalytic activity.

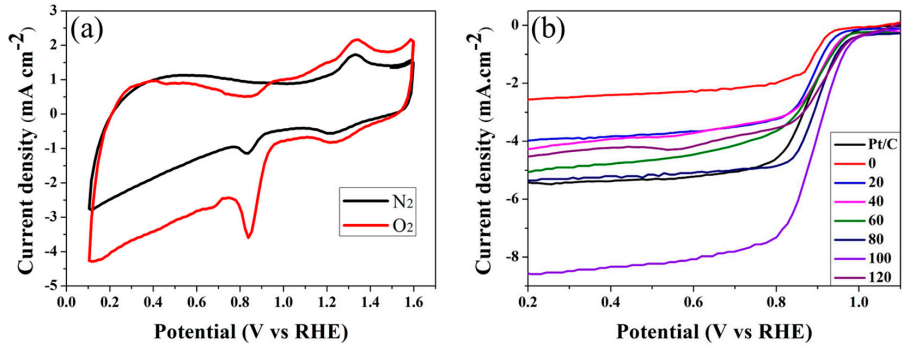

Figure 7. (**a**) Cyclic voltammetries (CVs) of Co-bpdc/MWCNTs-100; and (**b**) Oxygen reduction reaction (ORR) polarization curves of 20% Pt/C and Co-bpdc/MWCNTs catalysts with different contents of MWCNTs in 0.1 M KOH (Scan rate: 10 mV s^{-1}; rotation rate: 1600 rpm).

To better understand the role of cobalt atoms in these catalysts, we acidified the Co-bpdc/MWCNTs-100 catalyst to retain the cobalt atoms in the catalyst. Figure 8a shows that the catalytic activity of the acidified catalyst is not as good as that of Co-bpdc/MWCNTs-100, an indication that the cobalt atoms in the catalyst affect the oxygen reduction reaction. In addition, based on the ORR polarization curves of Co-bpdc/MWCNTs-100 and commercial Pt/C catalyst, the corresponding Tafel plots are shown in Figure 8b. The Tafel plot of Co-bpdc/MWCNTs-100 was determined to be 99.6 mV dec^{-1}, which is close to commercial Pt/C catalyst (96.6 mV dec^{-1}), indicating a similar reaction mechanism to the commercial Pt/C catalyst [41].

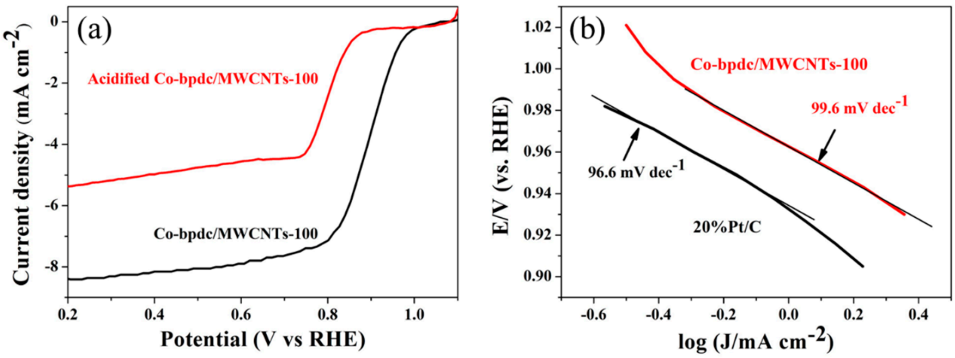

Figure 8. (**a**) ORR polarization curves of Co-bpdc/MWCNTs-100 and acidified Co-bpdc/MWCNTs-100 in 0.1 M KOH (Scan rate: 10 mV s^{-1}; rotation rate: 1600 rpm); (**b**) Tafel plots of 20% Pt/C and Co-bpdc/MWCNTs-100 in 0.1 M KOH.

It can be deduced that the nitrogen content is not the only factor that can affect the electrocatalytic activity of the prepared catalysts. The addition of MWCNTs allows the cobalt nanoparticles to distribute more uniformly, thus allowing the transmission of oxygen and electrolytes to the catalyst surface, thereby increasing the electrocatalytic activity towards the oxygen reduction reaction.

To further understand the reaction mechanism toward ORR in alkaline solution, the polarization curves of Co-bpdc/MWCNTs-100 at different rotating speeds are plotted in Figure 9a, and the corresponding Koutecky–Levich (K–L) plots are shown in Figure 9b. The polarization curves of Co-bpdc/MWCNTs-100 at different rotating speeds have the same initial reduction potential, but the current density increases with the increase of rotating speed. The K–L plots show excellent linearity and near coincidence in alkaline solution, indicating that the reactions on Co-bpdc/MWCNTs-100 follow first-order reaction kinetics and the electron transfer numbers (n) at different potentials are similar. The electron transfer numbers of the standard commercial Pt/C catalyst should be 4 [37]. The electron transfer numbers of Co-bpdc/MWCNTs-100 at different potentials were calculated to be in the range of 3.92–4.00 in an alkaline solution, with an average value of 3.97, which is very close to 4. These results indicate that the catalysts we prepared favor the 4-electron ORR process.

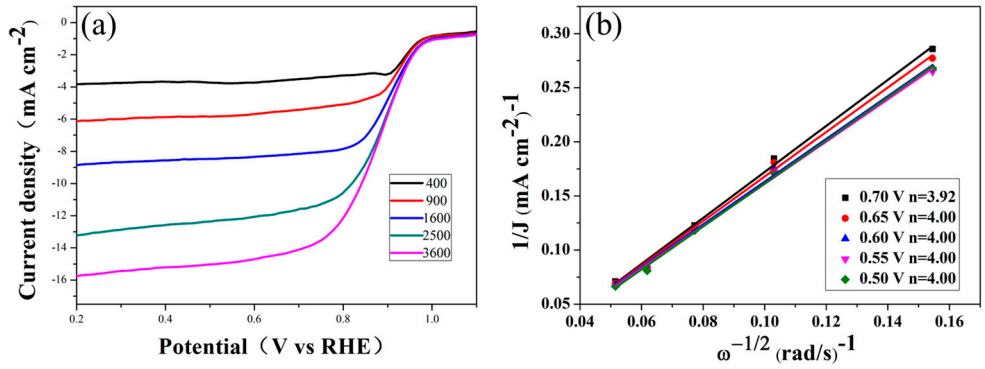

Figure 9. (**a**) ORR polarization curves of Co-bpdc/MWCNTs-100 at various rotating rates in 0.1 M KOH (scan rate: 10 mV s^{-1}); and (**b**) Koutecky–Levich plots of Co-bpdc/MWCNTs-100 at various potentials.

The RRDE measurements are shown in Figure 10. The measured H_2O_2 yields of Co-bpdc/MWCNTs-100 are below ~5% over the potential range of 0.15 V–1.0 V, and the electron transfer numbers are close to 4.0, consistent with the results calculated from the Koutecky–Levich equation based on the RDE measurements. The above results indicate that the prepared catalysts mainly favor the 4-electron ORR process.

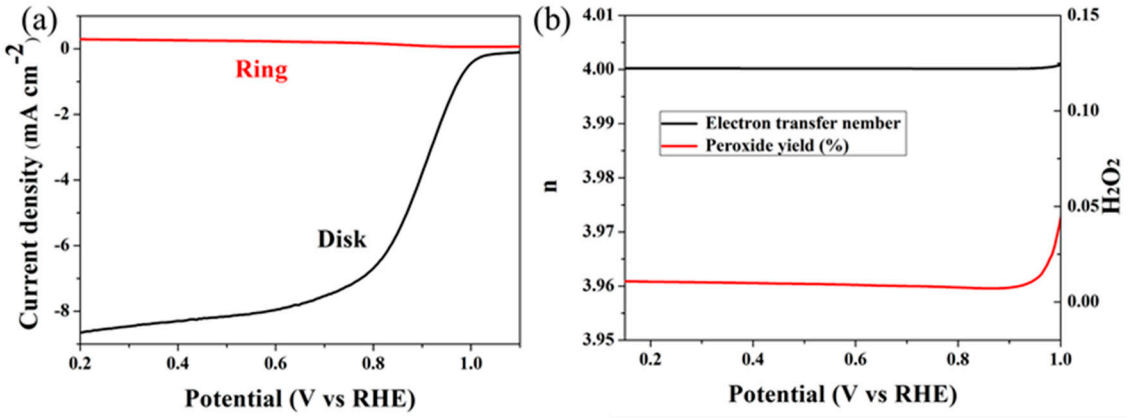

Figure 10. (**a**) Rotating ring-disk electron (RRDE) curve of Co-bpdc/MWCNTs-100 at 1600 rpm; and (**b**) electron transfer number and peroxide yield obtained at various potentials from RRDE curves.

The specific surface activity (SSA) values of Co-bpdc/MWCNTs-100 in the alkaline solution are obtained by the following equation:

$$\mathrm{SSA} = \frac{j_k}{m_{EC} - A_{BET}} \quad (7)$$

Here, j_k is the ORR kinetic current obtained on K–L plots at 0.90 V vs. RHE. m_{EC} is the Co-bpdc/MWCNTs-100 mass deposited on the RRDE tip and the A_{BET} is the BET area of Co-bpdc/MWCNTs-100 [42]. It was calculated that j_k is 0.511 mA cm^{-2} and m_{EC} of Co-bpdc/MWCNTs-100 is 0.408 mg cm^{-2}. The SSA of Co-bpdc/MWCNTs-100 is 0.57 μg cm^{-2}. The SSA of Co-bpdc/MWCNTs-100 is almost three orders of magnitude lower than the Pt/C Refs. [42,43].

The probable intrinsic performance of the active sites is as follows: the ORR process in the alkaline solution can be rationalized considering that (a) O_2 is absorbed on the Co nanoparticles; (b) O_2 is absorbed on the surface of Co-bpdc/MWCNTs-100. At the low ORR overpotentials, (b) the process is inhibited and (a) the process takes place on the Co nanoparticles of Co-bpdc/MWCNTs-100, which favor the 4-electron ORR process. When the ORR overpotentials exceed 9.0 V, Co-bpdc/MWCNTs-100 favor the 4-electron ORR process and 2-electron ORR process simultaneously, which could produce the H_2O_2. Finally, H_2O_2 is reduced to water on the surface of Co-bpdc/MWCNTs-100.

The electrocatalytic stability of Co-bpdc/MWCNTs-100 was assessed by the repetitive cycles in the range 0.5–1.5 V (at a scan rate of 100 mV s^{-1}). The polarization curve of Co-bpdc/MWCNTs-100 after 5000 cycles and the initial polarization curve of Co-bpdc/MWCNTs-100 are shown in Figure 11. The initial reduction potential does not decrease significantly and the half-wave potential of Co-bpdc/MWCNTs-100 shows only a negative shift of 5 mV. In addition, in the potential range of 0.4–0.7 V, the polarization curve after 5000 cycles shows an even higher current density than the initial polarization curve. These results indicate that Co-bpdc/MWCNTs-100 has a good ORR stability. The outstanding catalytic activity and stability of Co-bpdc/MWCNT composites make it a promising ORR electrocatalyst.

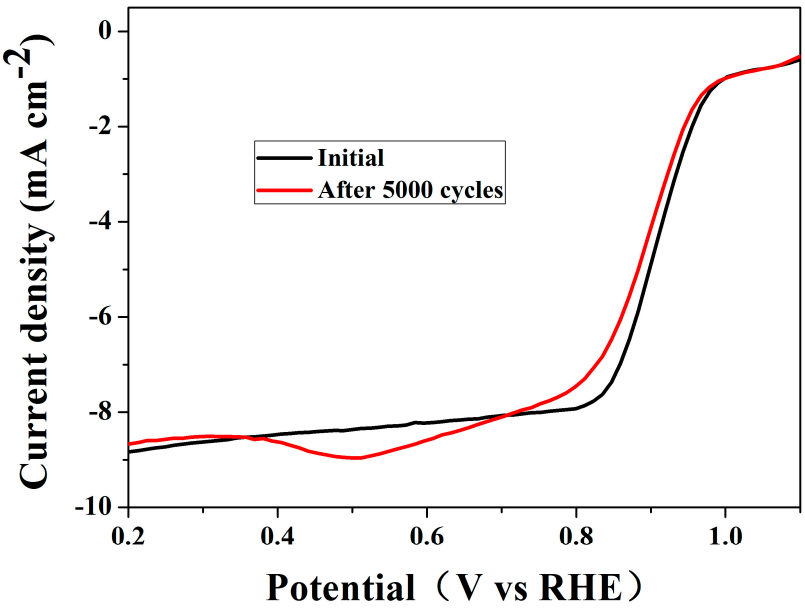

Figure 11. ORR polarization curves at 0 and 5000 cycles for Co-bpdc/MWCNTs-100.

4. Materials and Methods

4.1. Catalyst Preparation

Preparation of H_2bpdc. Phenanthroline (8 g), potassium permanganate (19 g) and sodium hydroxide (3.2 g) were added into 300 mL of deionized water in a flask. The mixture was heated at 98 °C for 3 h to obtain a purple black turbid liquid and a dark brown precipitate. A dark yellow transparent liquid was obtained by filtration. The filtrate was concentrated by evaporation to 150 mL and hydrochloric acid was added to adjust the pH to 2.0–2.5, resulting in a large amount of white precipitate after 24 h. Finally, the precipitate was collected by filtration and washed with deionized water to give the organic ligand (H_2bpdc).

Preparation of Co-bpdc. $Co(NO_3)_2.6H_2O$ (0.291 g) and H_2bpdc (0.244 g) were ultrasonically dissolved in 40 mL of a solution of ethanol (V_{water}:$V_{ethanol}$ = 2:1), NaOH was added to adjust the pH to 6, and the mixture was heated and stirred for 5 h. The resulting orange crystals were collected by filtration, washed with deionized water, and dried in a dryer.

Preparation of Co-bpdc/MWCNTs composites. $Co(NO_3)_2{\cdot}6H_2O$ (0.291 g) and H_2bpdc (0.244 g) were ultrasonically dissolved in 40 mL of a solution of ethanol in water (V_{water}:$V_{ethanol}$ = 2:1), and then a NaOH solution was added to adjust the pH to 6. Different amounts of acid-treated MWCNTs (20, 40, 60, 80, 100, and 120 mg) were added the mixture solution, heated, and stirred for 5 h. The resulting crystals were collected by filtration, washed with deionized water, and dried in a dryer.

Preparation of catalysts. The above prepared Co-bpdc and Co-bpdc/MWCNTs composites were transferred into a tube furnace and exposed to a flow of nitrogen for 30 min. The furnace was heated to 600 °C at a rate of 4 °C min^{-1} for 4 h and then cooled down to room temperature. Finally, the catalysts were ground and sealed.

4.2. Materials Characterization

X-ray diffraction (XRD) was performed on a Bruker D8 Advanced diffractometer (BrukerAXSGmbH, Karlsruhe, Germany) with Cu Kα radiation (λ = 1.5406 Å) to obtain the crystalline structures of catalysts. Raman spectra were obtained on a Raman Spectrometer (Thermo Fisher Scientific, Waltham, MA, USA) equipped with a Leica DMLM microscope and a 514 nm Ar^+ ion laser as an excitation source. The microstructure and morphology of the catalysts were observed under a JEOL JEM-3010HR and a JEM-2100 microscope (Japan electronics Co., Ltd., Tokyo, Japan). X-ray photoelectron spectroscopy (XPS) was performed on a Thermo Fisher Scientific ESCALAB 250 imaging photoelectron spectrometer (Thermo Fisher Scientific, Waltham, MA, USA). The specific surface area and the pore size distribution are measured by the BET model and Barrette–Joynere–Halenda (BJH) model, respectively, on an ASAP 2460 instrument (Quantachrome, South San Francisco, CA, USA).

4.3. Electrochemical Test

The electrochemical measurements were obtained at room temperature on an IM6ex electrochemical workstation manufactured by ZAHNER ENNIUM (Kronach, Germany) with a standard three-electrode system. The glassy carbon rotating disk electrode (5 mm in diameter) was used as the working electrode. A platinum electrode and an $Hg/HgSO_4$ electrode with saturated KCl solution were used as the counter and reference electrodes, respectively. All the potentials measured were converted to reversible hydrogen electrode (RHE) scale. Cyclic voltammetry (CV) and linear sweeping voltammetry (LSV) were performed with a rotating disk electrode (RDE) and a rotating ring disk electrode (RRDE) on samples in 0.1 M KOH solution saturated with N_2 or O_2 (versus RHE). The preparation process of catalyst ink is as follows: 4 mg of the catalysts and 10 μL of 0.5 wt % Nafion solution were dispersed in 1 mL of isopropanol solution ($V_{isopropanol}$:V_{H2O} = 2:3) ultrasonically. We took 20 μL of the catalyst ink (containing 80 μg of catalysts) and dropped it on the surface of the glassy carbon electrode, and then the catalyst ink was naturally dried at room temperature before the measurement.

5. Conclusions

We have synthesized a novel MOF material (named as Co-bpdc) and applied it to a series of non-precious metal catalysts for fuel cells. The prepared catalysts show higher ORR catalytic activity than the commercial Pt/C catalyst in alkaline solution, and Co-bpdc/MWCNTs-100 shows the highest ORR catalytic activity of the series, with its initial reduction potential and half-wave potential reaching 0.99 V and 0.92 V, respectively, in 0.1 M KOH solution. Moreover, the catalysts favor the 4-electron ORR process in alkaline solution, and exhibit higher stability in alkaline solution than the commercial Pt/C catalyst. The addition of MWCNTs can enhance the electrocatalytic activity. In addition, this work provides a novel idea for the synthesis of MOF materials as precursors to prepare ORR electrocatalysts. Our results indicate that MOF materials have great potential in non-precious catalysts for full cell applications.

Acknowledgments: The authors gratefully acknowledge the financial support from the National Key Research and Development Program of China (No. 2016YFB0101203), Beijing Municipal Science and Technology program (No. Z171100000917019), the National Natural Science Foundation of China (No. 21376022 and 21776014), the International S&T Cooperation Program of China (No. 2013DFA51860) and the Fundamental Research Funds for the Central Universities (No. JC1504).

Author Contributions: Ke Li performed a literature review, categorized the electrocatalysts in the introduction, did the research work and the main part of data analysis, and wrote the main part of the current work. Minglin Chen and Hehuan Cao corrected the English, helped with the part of data analysis and wrote part of this work. Fanghui Wang and Hong Zhu wrote part of this work, corrected the English grammar and syntax and supervised the whole work.

Conflicts of Interest: The authors declare no conflict of interest.

References

1. Qiao, X.C.; Liao, S.J.; Zheng, R.P.; Deng, Y.J.; Song, H.Y.; Du, L. Cobalt and nitrogen co-doped graphene with inserted carbon nanospheres as an efficient bifunctional electrocatalyst for oxygen reduction and evolution. *ACS Sustain. Chem. Eng.* **2016**, *4*, 4131–4136. [CrossRef]
2. Chu, S.; Majumdar, A. Opportunities and challenges for a sustainable energy future. *Nature* **2012**, *488*, 294–303. [CrossRef] [PubMed]
3. Lai, Q.X.; Su, Q.; Gao, Q.W.; Liang, Y.Y.; Wang, Y.X.; Yang, Z.; Zhang, X.G.; He, J.P.; Tong, H. In situ self-scrificed template synthesis of Fe-N/G catalysts for enhanced oxygen reduction. *ACS Appl. Mater. Interfaces* **2015**, *7*, 18170–18178. [CrossRef] [PubMed]
4. Xia, B.Y.; Yan, Y.; Wang, X.; Lou, X.W. Recent progress on graphene-based hybrid electrocatalysts. *Mater. Horiz.* **2014**, *1*, 379–399. [CrossRef]
5. Chen, A.; Holt-Hindle, P. Platinum-based nanostructured materials: Synthesis, properties, and applications. *Chem. Rev.* **2010**, *110*, 3767–3804. [CrossRef] [PubMed]
6. Zhang, Y.; Huang, L.B.; Jiang, W.J.; Zhang, X.; Chen, Y.Y.; Wei, Z.D.; Wan, L.J.; Hu, J.S. Sodium chloride-assisted green synthesis of a 3D Fe–N–C hybrid as a highly active electrocatalyst for the oxygen reduction reaction. *J. Mater. Chem. A* **2016**, *4*, 7781–7787. [CrossRef]
7. Wang, Y.; Nie, Y.; Ding, W.; Chen, S.G.; Xiong, K.; Qi, X.Q.; Zhang, Y.; Wang, J.; Wei, Z.D. Unification of catalytic oxygen reduction and hydrogen evolution reactions: Highly dispersive Co nanoparticles encapsulated inside Co and nitrogen co-doped carbon. *Chem. Commun.* **2015**, *51*, 8942–8945. [CrossRef] [PubMed]
8. Shang, L.; Yu, H.J.; Huang, X.; Bian, T.; Shi, R.; Zhao, Y.F.; Waterhouse, G.I.N.; Wu, L.Z.; Tung, C.H.; Zhang, T.R. Well-dispersed ZIF-derived Co,N-co-doped carbon nanoframes through mesoporous-silica-protected calcination as efficient oxygen reduction electrocatalysts. *Adv. Mater.* **2016**, *28*, 1668–1674. [CrossRef] [PubMed]
9. Shao, M.H.; Chang, Q.W.; Dodelet, J.P.; Chenitz, R. Recent advances in electrocatalysts for oxygen reduction reaction. *Chem. Rev.* **2016**, *116*, 3594–3657. [CrossRef] [PubMed]
10. Hu, K.; Tao, L.; Liu, D.D.; Huo, J.; Wang, S.Y. Sulfur-doped Fe/N/C nanosheets as highly efficient electrocatalysts for oxygen reduction reaction. *ACS Appl. Mater. Interfaces* **2016**, *8*, 19379–19385. [CrossRef] [PubMed]

11. Yao, Y.; Xiao, H.; Wang, P.; Su, P.P.; Shao, Z.G.; Yang, Q.H. CNTs@Fe–N–C core–shell nanostructures as active electrocatalyst for oxygen reduction. *J. Mater. Chem. A* **2014**, *2*, 11768–11775. [CrossRef]
12. Zhu, Y.S.; Zhang, B.S.; Liu, X.; Wang, D.W.; Su, D.S. Unravelling the structure of electrocatalytically active Fe-N complexes in carbon for the oxygen reduction reaction. *Angew. Chem. Int. Ed.* **2014**, *53*, 10673–10677. [CrossRef] [PubMed]
13. Choi, C.H.; Baldizzone, C.; Polymeros, G.; Pizzutilo, E.; Kasian, O.; Schuppert, A.K.; Sahraie, N.R.; Sougrati, M.T.; Mayrhofer, K.J.J.; Jaouen, F. Minimizing operando demetallation of Fe-N-C electrocatalysts in acidic medium. *ACS Catal.* **2016**, *6*, 3136–3146. [CrossRef]
14. Brouzgou, A.; Song, S.Q.; Liang, Z.X.; Tsiakaras, P. Non-precious electrocatalysts for oxygen reduction reaction in alkaline media: Latest achievements on novel carbon materials. *Catalysts* **2016**, *6*, 159. [CrossRef]
15. Kadam, P.D.; Chuan, H.H. Erratum to: Rectocutaneous fistula with transmigration of the suture: A rare delayed complication of vault fixation with the sacrospinous ligament. *Int. Urogynecol. J.* **2016**, *27*, 505. [CrossRef] [PubMed]
16. Proietti, E.; Jaouen, F.; Lefèvre, M.; Larouche, N.; Tian, J.; Herranz, J.; Dodelet, J.P. Iron-based cathode catalyst with enhanced power density in polymer electrolyte membrane fuel cells. *Nat. Commun.* **2011**, *2*, 416. [CrossRef] [PubMed]
17. Nabae, Y.; Nagata, S.; Hayakawa, T.; Niwa, H.; Harada, Y.; Oshima, M.; Isoda, A.; Matsunaga, A.; Tanaka, K.; Aoki, T. Pt-free carbon-based fuel cell catalyst prepared from spherical polyimide for enhanced oxygen diffusion. *Sci. Rep.* **2016**, *6*, 23276. [CrossRef] [PubMed]
18. Zhang, S.L.; Zhang, Y.; Jiang, W.J.; Liu, X.; Xu, S.L.; Huo, R.J.; Zhang, F.Z.; Hu, J.S. Co@N-CNTs derived from triple-role CoAl-layered double hydroxide as an efficient catalyst for oxygen reduction reaction. *Carbon* **2016**, *107*, 162–170. [CrossRef]
19. Jahnke, H.; Schönborn, M.; Zimmermann, G. Organic dyestuffs as catalysts for fuel cells. *Top. Curr. Chem.* **1976**, *61*, 133–181. [PubMed]
20. Ferrero, G.A.; Preuss, K.; Marinovic, A.; Jorge, A.B.; Mansor, N.; Brett, D.J.L.; Fuertes, A.B.; Sevilla, M.; Titirici, M.M. Fe-N-doped carbon capsules with outstanding electrochemical performance and stability for the oxygen reduction reaction in both acid and alkaline conditions. *ACS Nano* **2016**, *10*, 5922–5932. [CrossRef] [PubMed]
21. Zhou, D.; Yang, L.P.; Yu, L.H.; Kong, J.H.; Yao, X.Y.; Liu, W.S.; Xua, Z.C.; Lu, X.H. Fe/N/C hollow nanospheres by Fe(iii)-dopamine complexation-assisted one-pot doping as nonprecious-metal electrocatalysts for oxygen reduction. *Nanoscale* **2015**, *7*, 1501–1509. [CrossRef] [PubMed]
22. Yu, H.Y.; Fisher, A.; Cheng, D.J.; Cao, D.P. Cu,N-codoped hierarchical porous carbons as electrocatalysts for oxygen reduction reaction. *ACS Appl. Mater. Interfaces* **2016**, *8*, 21431–21439. [CrossRef] [PubMed]
23. Fu, X.G.; Choi, J.Y.; Zamani, P.Y.; Jiang, G.P.; Hoque, M.A.; Hassan, F.M.; Chen, Z.W. Co-N decorated hierarchically porous graphene aerogel for efficient oxygen reduction reaction in acid. *ACS Appl. Mater. Interfaces* **2016**, *8*, 6488–6495. [CrossRef] [PubMed]
24. Zhang, G.; Lu, W.T.; Cao, F.F.; Xiao, Z.D.; Zheng, X.S. N-doped graphene coupled with Co nanoparticles as an efficient electrocatalyst for oxygen reduction in alkaline media. *J. Power Sources* **2016**, *302*, 114–125. [CrossRef]
25. Zhu, H.; Sun, Z.N.; Chen, M.L.; Cao, H.H.; Li, K.; Cai, Y.Z.; Wang, F.H. Highly porous composite based on tungsten carbide and N-doped carbon aerogels for electrocatalyzing oxygen reduction reaction in acidic and alkaline media. *Electrochim. Acta* **2017**, *236*, 154–160. [CrossRef]
26. Zhou, X.J.; Bai, Z.Y.; Wu, M.J.; Qiao, J.L.; Chen, Z.W. 3-Dimensional porous N-doped graphene foam as a non-precious catalyst for the oxygen reduction reaction. *J. Mater. Chem. A* **2015**, *3*, 3343–3350. [CrossRef]
27. Hao, J.H.; Yang, W.S.; Zhang, Z.; Tang, J.L. Metal-organic frameworks derived CoxFe1-xP nanocubes for electrochemical hydrogen evolution. *Nanoscale* **2015**, *7*, 11055–11062. [CrossRef] [PubMed]
28. Huskić, I.; Pekov, I.V.; Krivovichev, S.V.; Friščić, T. Minerals with metal-organic framework structures. *Sci. Adv.* **2016**, *2*, e1600621. [CrossRef] [PubMed]
29. You, S.J.; Gong, X.B.; Wang, W.; Qi, D.P.; Wang, X.H.; Chen, X.D.; Ren, N.Q. Enhanced cathodic oxygen reduction and power production of microbial fuel cell based on noble-metal-free electrocatalyst derived from metal-organic frameworks. *Adv. Energy Mater.* **2016**, *6*, 1501497. [CrossRef]

30. Zhu, Q.L.; Xia, W.; Akita, T.; Zou, R.Q.; Xu, Q. Metal-organic framework-derived honeycomb-like open porous nanostructures as precious-metal-free catalysts for highly efficient oxygen electroreduction. *Adv. Mater.* **2016**, *28*, 6391–6398. [CrossRef] [PubMed]
31. Zhang, Y.F.; Bo, X.J.; Nsabimana, A.; Han, C.; Li, M.; Guo, L.P. Electrocatalytically active cobalt-based metal–organic framework with incorporated macroporous carbon composite for electrochemical applications. *J. Mater. Chem. A* **2015**, *3*, 732–738. [CrossRef]
32. Zhao, H.X.; Zou, Q.; Sun, S.K.; Yu, C.S.; Zhang, X.J.; Lia, R.J.; Fu, Y.Y. The ranostic metal–organic framework core–shell composites for magnetic resonance imaging and drug delivery. *Chem. Sci.* **2016**, *7*, 5294–5301. [CrossRef]
33. Song, Y.H.; Li, X.; Sun, L.L.; Wang, L. Metal/metal oxide nanostructures derived from metal–organic frameworks. *RSC Adv.* **2015**, *5*, 7267–7279. [CrossRef]
34. Mahmood, A.; Guo, W.H.; Tabassum, H.; Zou, R.Q. Metal-organic framework-based nanomaterials for electrocatalysis. *Adv. Energy Mater.* **2016**, *6*, 1600423. [CrossRef]
35. Li, X.Z.; Fang, Y.Y.; Lin, X.Q.; Tian, M.; An, X.C.; Fu, Y.; Li, R.; Jin, J.; Ma, J. MOF derived Co_3O_4nanoparticles embedded in N-doped mesoporous carbon layer/MWCNT hybrids: Extraordinary bi-functional electrocatalysts for OER and ORR. *J. Mater. Chem. A* **2015**, *3*, 17392–17402. [CrossRef]
36. Maghsodi, A.; Milani, H.M.; Dehghani, M.M.; Kheirmand, M.; Samiee, L.; Shoghi, F.; Kameli, M. Exploration of bimetallic Pt-Pd/C nanoparticles as an electrocatalyst for oxygen reduction reaction. *Appl. Surf. Sci.* **2011**, *257*, 6353–6357. [CrossRef]
37. Yi, L.H.; Liu, L.; Liu, X.; Wang, X.Y.; Yi, W.; He, P.Y.; Wang, X.Y. Carbon-supported Pt-Co nanoparticles as anode catalyst for direct borohydride-hydrogen peroxide fuel cell: Electrocatalysis and fuel cell performance. *Int. J. Hydrog. Energy* **2012**, *37*, 12650–12658. [CrossRef]
38. Geng, D.S.; Chen, Y.; Chen, Y.G.; Li, Y.L.; Li, R.Y.; Sun, X.L.; Ye, S.Y.; Knights, S. High oxygen-reduction activity and durability of nitrogen-doped graphene. *Energy Environ. Sci.* **2011**, *4*, 760–764. [CrossRef]
39. Xia, W.; Zou, R.Q.; An, L.; Xia, D.G.; Guo, S.J. A metal–organic framework route to in situ encapsulation of $Co@Co_3O_4@C$ core@bishell nanoparticles into a highly ordered porous carbon matrix for oxygen reduction. *Energy Environ. Sci.* **2015**, *8*, 568–576. [CrossRef]
40. Jiang, H.L.; Yao, Y.F.; Zhu, Y.H.; Liu, Y.Y.; Su, Y.H.; Yang, X.L.; Li, C.Z. Iron carbide nanoparticles encapsulated in mesoporous Fe-N-doped graphene-like carbon hybrids as efficient bifunctional oxygen electrocatalysts. *ACS Appl. Mater. Interfaces* **2015**, *7*, 21511–21520. [CrossRef] [PubMed]
41. Zhao, P.P.; Xu, W.; Hua, X.; Luo, W.; Chen, S.L.; Cheng, G.Z. Facile synthesis of a N-doped Fe3C@CNT/porous carbon hybrid for an advanced oxygen reduction and water oxidation electrocatalyst. *J. Phys. Chem. C* **2016**, *120*, 11006–11013. [CrossRef]
42. Vezzù, K.; Delpeuch, A.B.; Negro, E.; Polizzi, S.; Nawn, G.; Bertasi, F.; Pagot, G.; Artyushkova, K.; Atanassov, P.; Noto, V.D. Fe-carbon nitride "core-shell" electrocatalysts for the oxygen reduction reaction. *Electrochim. Acta* **2016**, *222*, 1778–1791. [CrossRef]
43. Negro, E.; Polizzi, S.; Vezzu, K.; Toniolo, L.; Cavinato, G.; Noto, V.D. Interplay between morphology and elecrtrochemical performance of "core-shell" electrocatalysts for oxygen reduction reaction based on a PtNix carbon nitride "shell" and a pyrolyzed polyketone nanoball "core". *Int. J. Hydrog. Energy* **2014**, *39*, 2828–2841. [CrossRef]